ORIGINAL ARTICLE

Journal Section

Spatial Photo-Patterning of Nematic Liquid Crystal Pretilt and its Application in Fabricating Flat Gradient-Index Lenses

Alvin Modin[1] | **Robert L. Leheny**[1] | **Francesca Serra**[1,2]

[1]Department of Physics and Astronomy, Johns Hopkins University, Baltimore, MD 21218, USA

[2]Department of Physics, Chemistry, and Pharmacy, University of Southern Denmark, Odense, DK-5230 Denmark

Correspondence
Francesca Serra or Alvin Modin
Email: serra@sdu.dk or modin@jhu.edu

Liquid crystals offer a dynamic platform for developing advanced photonics and soft actuation systems due to their unique and facile tunability and reconfigurability. Achieving precise spatial patterning of the liquid crystal alignment is critical to developing electro-optical devices, programmable origami, directed colloidal assembly, and controlling active matter. Here, we demonstrate a simple method to achieve continuous three-dimensional control of the directions of liquid crystal mesogens using a two-step photo-exposure process. In the first step, polarized light sets the orientation in the plane of confining substrates; the second step uses unpolarized light of a prescribed dose to set the out-of-plane orientation. The method enables smoothly varying orientational patterns with sub-micrometer precision. As a demonstration, we design gradient-index lenses with parabolic refractive index profiles that remain stable without external electric fields. We characterize the lenses' focal length and sensitivity to light polarization through experimental and numerical methods. Our findings pave the way for developing next-generation photonic devices and actuated materials, with potential applications in molecular self-assembly, re-configurable optics, and responsive matter.

KEYWORDS
liquid crystal devices, microlenses, nematic pretilt, photoalignment

1. Introduction

Liquid crystals (LCs) are versatile, adaptive materials with tunable physical properties arising from the order of their rod-like molecules. Nematic LCs, in particular, are characterized by a director – a unit-vector, $\hat{n}(\mathbf{r})$ – that delineates the local orientational alignment of the LC molecules, known as mesogens. Historically, $\hat{n}(\mathbf{r})$ has been controlled by using electric fields [1], shear flows [2], and rubbed polymer coatings [3]. These methods predominantly favor uniaxial alignment, where mesogens are all oriented in the same direction over large regions.

Photoalignment has emerged as a powerful alignment technique in research and industrial settings, allowing microscopic spatial patterning of the LC director [4, 5]. The method employs a substrate with a thin film of photosensitive dye that is selectively illuminated with polarized light to tailor the azimuthal (in-plane) orientation of $\hat{n}(\mathbf{r})$. When irradiated with polarized light, the photosensitive molecules on the substrate, typically

derivatives of azobenzene, undergo trans-cis isomerization. In time, they progressively orient their long axes (and thus their dipoles) perpendicularly to the local light polarization [6, 7], setting the preferred alignment or "anchoring" direction of $\hat{n}(\mathbf{r})$ in the liquid crystal adjacent to the substrate [8, 9, 10]. Various approaches exist to pattern the alignment. Direct laser writing [11, 12], plasmonic masks [13, 14], and digital micromirror devices [15] offer static and dynamic options to imprint intricate patterns as anchoring conditions for LCs. These approaches have been used for a variety of applications, including LC vortices capable of steering light [16], phase-based flat microlenses [17], and actuators made of liquid-crystal elastomers [18, 19, 20].

Existing photoalignment techniques allow for continuous variation of the in-plane alignment to be imposed. Control over the director's pretilt (out-of-plane, polar) angle with photoalignment is more complicated. Presently, only discrete LC domains can be tailored to have a varying pretilt alignment by using multi-step processes involving stacked alignment layers [21], photo-cross linking polymer layers [22, 23], and patterned electrodes [24, 2]. The ability to impose a continuous spatial variation in the pretilt would significantly expand the application potential of photoaligned LCs, such as by increasing the accessible degrees of freedom for controlling the actuated shapes of liquid crystal elastomers [25] or for creating new phased-based LC optical devices [17, 26, 27].

Previous work [9] has demonstrated that photoalignment using unpolarized light can control the nematic pretilt angle. Varying the incident angle of unpolarized light with respect to the sample plane of an LC cell, photosensitive azo-dye Brilliant Yellow (BY) (see *Supplementary Information* for chemical structure) has been shown to re-orient to generate an exposure-dependent pretilt in $\hat{n}(\mathbf{r})$ over a limited range of angles [28]. The out-of-plane alignment arises from the azo-molecules undergoing trans-cis-trans isomerization cycles, ultimately acquiring an out-of-plane angle as they align parallel to the light propagation direction. Filling the sample with LC broadens the range of achievable pretilt angles [29]. Since in these previous cases the technique relies on physically tilting the sample to generate oblique photo-exposures [30], finely controlled, spatially varying patterns of the pretilt angle are inaccessible. To date, navigating complex, multi-step processes has proven to be a significant barrier in achieving continuous, three-dimensional (3D) patterning of $\hat{n}(\mathbf{r})$.

Here we demonstrate an approach to achieve smooth, 3D variation in $\hat{n}(\mathbf{r})$ that employs a straightforward, two-step exposure process to photo-pattern the nematic pretilt (Figure 1). Notably, the technique can be implemented using only a microscope and standard optics. The photoalignment process involves an initial exposure with polarized light to set the in-plane director alignment, followed by a second exposure with unpolarized light, both normal to the substrate. By adjusting the exposure duration of the unpolarized light, the polar angle of the director can be precisely tuned over the full range from zero to 90°. The degree of pretilt depends on the total dose applied, independent of the light flux. Because the exposure time can be varied continuously as a function of position, the approach can create smooth variations of pretilt with arbitrary spatial profiles. To demonstrate this method, we design and fabricate gradient-index (GRIN) microlenses with parabolic refractive index profiles. The lenses are formed by a gradually varying, radially dependent director profile that is stable without needing an applied electric field. The lens properties are quantitatively consistent with our characterization of the imposed pretilt from diagnostic measurements, confirming the method's efficacy for developing next-generation optical and actuated materials.

2. Results and Discussion

2.1 Generating pretilt with two-step photoalignment

We use a two-step process to photo-pattern the azimuthal and polar orientation of $\hat{n}(\mathbf{r})$. Our strategy relies on exposing azo-dye films on glass substrates to unpolarized light in the presence of nematic LC, which has been shown to promote out-of-plane LC re-orientation [29]. To pattern the nematic, we use a custom-built photoalignment system [31] (see Figure 1 and the Experimental Section). LC cells are assembled out of indium tin

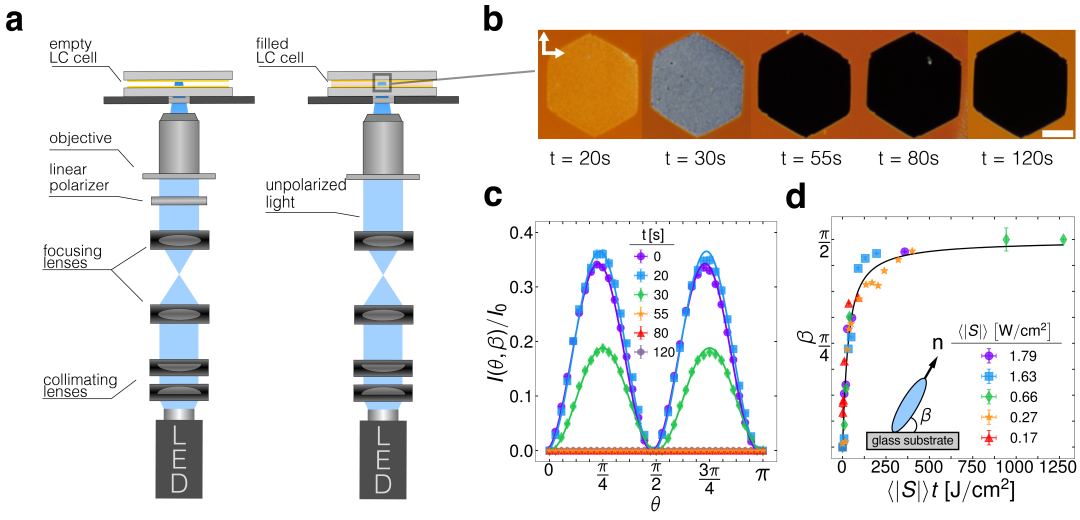

FIGURE 1 **Controlling nematic pretilt with unpolarized light.** **a**) Simplified schematic of the photoalignment apparatus to generate spatially varying pretilt. An empty LC cell with BY-coated substrates (left) is initially exposed to polarized light, setting the azimuthal anchoring direction for LC molecules. After the cell is filled with nematic LC (right), a region is re-exposed to unpolarized light, forcing the BY (and LC) molecules to re-align out-of-plane. **b**) When viewed under crossed-polarizers, the transmission of white light in each re-exposed region varies with the exposure time t of unpolarized light (scale bar: 30 μm). **c**) Rotating the sample by θ changes the relative transmitted light intensity $I(\theta,\beta)/I_0$ through the LC cell. The power flux of the light source is $\langle|S|\rangle = 1.63$ W $\cdot$ cm^{-2} and the wavelength $\lambda = 647$ nm. Solid lines are results from fits using Equation 1 to obtain β for different exposure times with $d = 2.81$ μm. Error bars represent the standard deviation of the transmitted light intensity in the re-exposed region for a given θ. **d**) Plotting β obtained with different $\langle|S|\rangle$ shows that the pretilt angle depends on the exposure energy and saturates at a maximum value of $\approx 90°$, independent of $\langle|S|\rangle$. The solid line is an empirical best fit to the data described in the text. Error bars correspond to the standard deviation of diagonal elements of the covariance matrix for the best-fit parameters.

oxide (ITO) glass substrates that have been spin-coated with a thin film of the photosensitive dye BY. When the empty cell is first illuminated with linearly polarized light, the BY molecules in the exposed region align themselves to be orthogonal to the light's polarization direction (see Figure 1a, left) [8]. We then fill the cell with 4-cyano-4'-pentylbiphenyl (5CB) in the isotropic phase ($T_{NI} \approx 41°$C) and subsequently allow it to cool to room temperature (T$\approx 24°$C), where the 5CB is nematic. The alignment of the BY molecules by the initial exposure creates a planar anchoring condition where the director is in-plane and perpendicular to the polarization direction. We subsequently remove the polarizer and illuminate regions of the sample with unpolarized light (Figure 1a, right). As the exposure time, t, increases, the molecules of the alignment layer tilt out of the plane, progressively aligning their absorption axes towards the propagation vector of the incident light while still maintaining the imprint of their initial in-plane alignment [8]. This orientation by the second exposure alters the LC anchoring condition, introducing a pretilt to the director that depends on the duration of the exposure.

Figure 1b displays several hexagonally shaped regions subjected to the two-step photoalignment with varying amounts of unpolarized light. Under crossed-polarizers, the resulting transmitted light intensity, I,

through each region holds quantitative information about the pretilt angle, β, due to the birefringence of 5CB. Specifically, at room temperature 5CB has a positive uni-axial optical response and birefringence, where $n_o = 1.524$ and $n_e = 1.708$ are the refractive indices perpendicular and parallel to the director, respectively [32]. As the duration of the second unpolarized light exposure changes from 20 s to 120 s, an overall qualitative decrease in the transmitted intensity is observed (Figure 1b). For incident light with wavelength λ, I is expected to change as a function of the in-plane orientation of $\hat{n}$ with respect to the analyzer, θ, as

$$I(\theta,\beta) = I_0 \sin^2(2(\theta+\phi)) \sin^2\left(\frac{\pi d}{\lambda}\left[n_{\text{eff}}(\beta) - n_o\right]\right). \quad (1)$$

The argument of the second term in Equation 1 captures the relative retardation experienced by the polarization component of the light parallel to the in-plane orientation of $\hat{n}$ when traveling through a nematic cell of thickness d, which for the sample in Figure 1b is $d = 2.81 \pm 0.04\ \mu$m. This term depends on the effective extraordinary index of refraction experienced by that component,

$$n_{\text{eff}}(\beta) = \frac{n_o n_e}{\sqrt{n_o^2 \cos^2\beta + n_e^2 \sin^2\beta}}. \quad (2)$$

We also introduce an additional parameter, ϕ, into Equation 1 to account for small errors in the alignment of $\hat{n}$ with respect to the polarizer, occurring when the sample is shifted to expose new regions. Note that I is not monotonic for increasing β and varies for a fixed θ in a way that depends on a combination of λ, d, and β (see *Supplementary Information* for detailed discussion). We use a narrow band-pass filter for all experiments to restrict $\lambda = 647 \pm 10$ nm. To obtain I_0, we measure the mean light intensity transmitted by an unexposed ($t = 0$) uniformly planar aligned region at various θ and fit Equation 1 to this data using the known values for d, λ, n_e, n_o. The resulting value for I_0 is then fixed for all subsequent fits for $t > 0$. Figure 1c shows $I(\theta,\beta)/I_0$ as a function of θ across six exposure times, each with a power flux of $\langle|S|\rangle = 1.63\ \text{W}\cdot\text{cm}^{-2}$. We obtain β for each exposure time by a two-parameter fit using Equation 1, allowing ϕ to vary. The resulting curves are shown in Figure 1c.

We find that β increases monotonically with increasing exposure time. Eventually, at long times, the pretilt saturates at $\beta_{\text{max}} \approx 90^\circ$ (Figure 1d). To investigate how β depends on the incident power flux, we conduct similar experiments at four different values of $\langle|S|\rangle$. Re-scaling the exposure time by $\langle|S|\rangle$ gives the energy dose received by each re-aligned region. The collapse of the data sets in Figure 1d reveals that for this range of fluxes, the variation of β depends only on the energy dose received [28]. Notably, the transmitted intensities in Figure 1c also follow the expected variation with θ, implying that the azimuthal alignment of $\hat{n}$ is preserved as β varies with the exposure to unpolarized light.

2.2 Crafting parabolic gradient-index lenses

This two-step illumination method for controlling β allows for specific regions to be illuminated with different amounts of unpolarized light. As a result, it enables diverse pretilt patterns within a sample to be facilely created without using physical masks or altering the sample orientation with respect to the incident light. Indeed, the method can create a continuously varying pretilt by smoothly tuning the exposure time across a region. As a practical demonstration of the technique, we craft micro-scale LC GRIN lenses to demonstrate the precision of this capability. The lenses have a β ranging from 0 to a peak of $\approx 90^\circ$ (Figure 2a) such that n_{eff} has a parabolic profile.

To fabricate a lens, we first apply linearly polarized light exposure to create a large rectangular region with uniform planar alignment. During the second exposure, an annular region of fixed outer radius R_o and time-dependent inner radius $R_i(t)$ is exposed to unpolarized light (Figure 2b). The inner radius continuously grows from zero so that the exposure time (and hence the resulting pretilt β) increases with increasing distance r from the center. Specifically, $R_i(t)$ is chosen to ensure the formation of a GRIN lens with radius R_L and parabolic index of refraction profile,

$$n_{\text{eff}}(r) = n_{\text{max}} - (\Delta n)\left(\frac{r}{R_L}\right)^2, \quad (3)$$

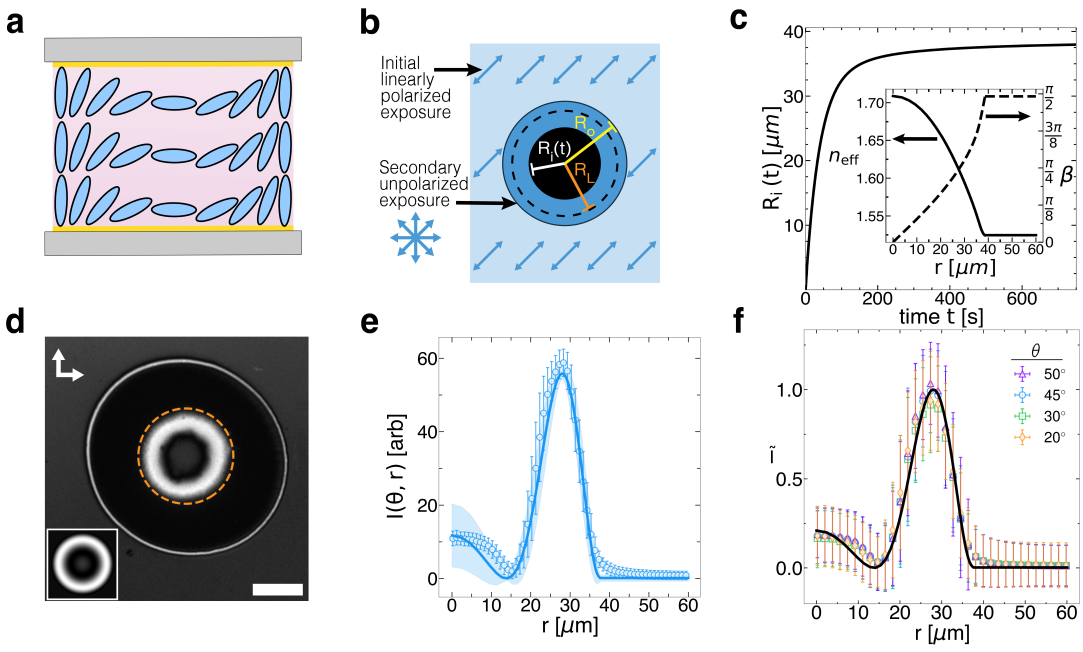

FIGURE 2 **Crafting gradient-index lenses by varying pretilt profile. a**) Schematic cross-section of an LC cell forming a gradient-index (GRIN) lens. **b**) The two-step photo-patterning process for varied pretilt. An initial rectangular region is illuminated with linearly polarized light (light blue region), ensuring uniform LC alignment. In a second exposure, unpolarized light illuminates an annular region (dark blue) with a time-dependent inner radius to vary the exposure time radially. **c**) The time-dependent inner radius, $R_i(t)$, leading to $\beta(r)$ (inset, dashed curve) and a parabolic $n_{eff}(r)$ (inset, solid curve) that create a lens with radius $R_L = 38\ \mu$m. **d**) Polarized-optical microscopy of a GRIN lens of radius $R_L = 38\ \mu$m (orange, dashed line). The lens radius R_L is smaller than the outer radius $R_o = 70\ \mu$m of the region exposed to unpolarized light. Inset: Predicted POM texture for a lens with radius R_L, reconstructed from Jones calculus from the director field defined by $\beta(r)$ (scale bar: 40 μm). **e**) Radial transmitted light intensity profile, $I(\theta, r)$, for $\theta = \pi/4$. The solid curve represents the theoretical model (Equation 4), with the shaded area indicating the associated uncertainty (see *Supplementary Information* for details). **f**) Accounting for θ and ϕ, $I(\theta, r)$ at different θ collapse onto a single curve defined by $\tilde{I} = I(\theta, r)/\sin^2(2(\theta + \phi))$.

where $\Delta n \equiv n_{max} - n_{min}$. Here, n_{min} corresponds to the minimum effective refractive index achieved at β_{max}. For the GRIN lens in Figure 2, our chosen values of n_{max} and n_{min} are simply n_e and n_o, respectively. We make R_L smaller than R_o so that the secondary exposure creates an annular region, $R_L < r < R_o$, around the lens with $\beta \approx \beta_{max}$. This configuration spatially separates the lens from the boundary with the surrounding area with planar anchoring.

This parabolic index of refraction profile is obtained through a pretilt profile $\beta(r)$ that we find by combining Equations 2 and 3 and solving numerically for β. To derive the corresponding form for $R_i(t)$, we fit the measurements of $\beta(t)$ (Figure 1d) at varying $\langle|S|\rangle$ using the empirical form $\beta(t) = \arctan\left([a\langle|S|\rangle t]^b\right)$. Here, a and b are free parameters, which we find to be $a = 3.097\ \text{cm}^2/\text{J}$, and $b = 0.87$ by non-linear least-square minimization. Combining these fitting parameters with the light flux used for lens fabrication, $\langle|S|\rangle = 0.51\ \text{W}\cdot\text{cm}^{-2}$, we numerically interpolate between $\beta(t)$ and $\beta(r)$ to derive a result for the exposure time as a function of r. This is then inverted to obtain $R_i(t)$ that generates the parabolic profile given by Equation 3 (Figure 2c). Figure 2d shows a polarized optical microscopy (POM) im-

age of a GRIN lens with $R_L = 38\ \mu$m fabricated in this way. The specific values of $\beta(r)$ and $R_i(t)$ for this lens are provided in a data repository.

To analyze the index of refraction profile of the lens, we measure its transmitted light intensity. As β increases with r, the transmitted intensity, described by Equation 1, becomes radially dependent:

$$I(\theta, r) = I_0 \sin^2(2(\theta + \phi)) \sin^2\left(\frac{\pi d}{\lambda}\left[n_{\text{eff}}(r) - n_o\right]\right). \quad (4)$$

For the lens in Figure 2d, $d = 4.06 \pm 0.08\ \mu$m, making $I(\theta, r)$ non-monotonic with increasing β and hence also with the distance from the lens center. The obtained POM textures qualitatively match those obtained using Jones matrix calculations for Equation 3 (see Experimental Section and Figure 2d, inset). Using the target profile of $n_{\text{eff}}(r)$ from Equation 3, we also calculated the expected $I(\theta, r)$ for various θ. Figure 2e displays measurements for $I(\theta, r)$ for $\theta = \pi/4$, which align well with the predictions given by Equation 4. The expected spatial variation in the pretilt is further validated by the data in Figure 2f. Here, results for $I(\theta, r)$ at different θ collapse onto a single curve defined by $\tilde{I} = I(\theta, r)/\sin^2(2(\theta + \phi))$, which depends solely on the LC lens's refractive properties. This consistency underscores the accuracy and precision with which we can smoothly tune $\beta(\mathbf{r})$ with this method.

2.3 Lens characterization

The GRIN lens described above is a converging lens. As the lens radius is much larger than λ, optical effects in an LC-based GRIN lens are well approximated by geometric optics. The focal length, f, can be obtained by considering the maximum angle of refraction experienced by light at the periphery of the lens, $\alpha_{\max} \approx \frac{d}{n_g}\frac{dn(r)}{dr}\big|_{r=R_L} = \frac{R_L}{f}$, where n_g is the index of refraction of the glass [33]. In terms of the lens radius, the focal length is given by,

$$\frac{f}{n_g} = \frac{R_L^2}{2\Delta n d}, \quad (5)$$

(see *Supplementary Information* for a detailed discussion).

Equation 5 establishes a correlation between a lens's focal length and Δn achieved through photoalignment. Therefore, testing the imaging properties of lenses provides an independent measurement of Δn. To do so, we measure f of GRIN lenses fabricated with radii ranging from $R_L = 24$ to $38\ \mu$m across samples with thicknesses ranging between $L = 2.32$ to $4.64\ \mu$m. We position a mask containing die-cut letters "JHU" in front of a light source on an upright microscope to serve as an object to image (Figure 3a). Our GRIN lens is set on a rotating stage and brought into focus. Lowering the stage causes the mask's image to appear in the microscope objective's focal plane. Since the distance from the mask to the lens is much larger than f, the magnitude of this measured displacement provides a direct measure of f/n_g (see *Supplementary Information* and Figure S3 for a detailed schematic and discussion). We observe a linear relation between the $2f/n_g$ and R_L^2/d (Figure 3b). The solid line in Figure 3b depicts the expected relationship with slope $1/\Delta n$ and $\Delta n = 0.184$ based on $\beta_{max} = 90°$, and $n_g = 1.5$.

It was previously shown that elliptical (non-toric) focal conic domains in smectic LCs form GRIN lenses sensitive to light polarization [34]. The same effect can also be seen in our nematic GRIN lenses. During exposure with unpolarized light, the in-plane orientation of $\hat{n}$ created during the initial photo-exposure remains fixed, as shown in Figure 1c. Therefore, only light incident on the GRIN lens with polarization direction along $\hat{n}$ should experience a refractive index gradient. Conversely, light polarized along the direction perpendicular to the in-plane alignment will experience only n_o and no gradient between the periphery and the center of the lens.

To demonstrate this characteristic, we rotate the lens by $\pi/2$ while keeping the image of the mask in focus, as depicted in Figure 3c (see also *Supplementary Movie* S1). The image's contrast diminishes when the orientation of the $\hat{n}$ changes from being parallel to perpendicular to the illumination's polarization direction. This property is a stable, equilibrium configuration of the LC, existing without any applied external fields. The birefringent properties of our photoaligned lenses indicate that only the out-of-plane tilting of the nematic director is responsible for modulating the refractive index, con-

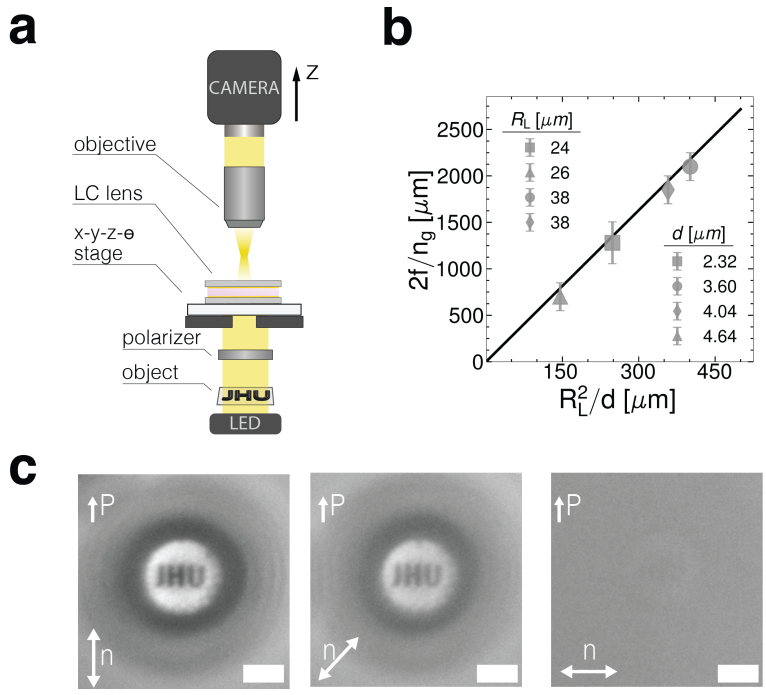

FIGURE 3 **Optical characterization of microlenses.** (**a**) Schematic illustrating the focal length measurement for a microlens. A "JHU" mask is positioned immediately after the light source. The sample is mounted on a rotating stage, enabling adjustment of the orientation of $\hat{n}$ relative to the light's polarization. (**b**) Lowering the lens brings the mask's image into focus within the microscope objective's focal plane. The quantity $2f/n_g$ exhibits a linear relationship with R_L^2/d. The solid line represents the predicted slope, $1/(\Delta n)$, with $\Delta n = 0.184$ derived from the peak value of β at $\beta(r = R_L)$. (**c**) Lensing is contingent upon the alignment of $\hat{n}$ with the illumination's polarization direction (P). When $\hat{n}$ is orthogonal to P, the microlens fails to form an image (scale bar: 20 μm).

firming that the in-plane component maintains its alignment direction during the second photo-exposure step. As $\hat{n}(\mathbf{r})$ is continuously varying throughout, the lens can be considered a spatially variant waveplate array, which can manipulate the polarization and phase of any incident light beam.

3. Conclusion

In this work, we introduce a new framework for achieving smoothly varying spatial patterning of the polar and azimuthal components of the LC director by a sequential combination of polarized and unpolarized light exposure. By exposing BY-coated substrates of a filled nematic LC cell to unpolarized light, the nematic director undergoes an out-of-plane re-orientation with a pretilt angle β that varies with the energy dose received. Our method circumvents the need for masks, stacked alignment layers, electric fields, or altering the sample's orientation relative to the light source, facilitating a high spatial resolution of the nematic pretilt. Our technique enables precise, continuous sub-microscale control of tilt angles with a basic microscope setup and employs a generalizable data analysis method. While we demonstrate our method for BY paired with 5CB, the technique can be generalized to other azo-based materials, provided that they are good alignment layers for the chosen liquid crystal and capable of generating an out-of-plane alignment (see *Supplementary Movie S2*, where a similar experiment is shown with 8CB). We hope our work will stimulate further research into the molecular mechanism governing azo-dye realignment dynamics.

To demonstrate the precision of our technique, we crafted GRIN lenses with parabolic refractive index profiles. Though our parabolic profile extends between n_e and n_o, our technique allows for the values of n_{max} and n_{min} in Equation 3 to be varied. As the pretilt depends only on the anchoring conditions at the alignment layer, the lenses remain stable without needing external electric fields. The optical characteristics of the lenses are in good agreement with those expected from our measurements of $\beta(t)$, and both quantitatively and qualitatively confirm that the secondary exposure with unpolarized light preserves the in-plane orientation of $\hat{n}$.

Beyond the demonstrated application to GRIN lens fabrication, this approach should facilitate the development of more broadly controllable liquid crystal elastomers [25], where the encoded pretilt biases actuation to specific deformation modes [35, 18]. In addition, our technique opens up the possibility of creating new optical instruments, including re-writable gradient index lenses and phase-based optical devices [26, 27], photoswitches [36], spatial light modulators [37], sensors [38], and polarimeters for minimally invasive clinical diagnosis [39]. Our GRIN lenses can be designed explicitly with pretilt profiles that function at low voltages, resulting in faster electro-optical modulation [40, 22]. The ability to smoothly vary the pretilt in LCs enables the design and fabrication of optical devices that precisely structure and shape light [39], improving the resolution in both augmented and virtual reality systems [41]. Furthermore, by varying specific boundary conditions, our method provides a platform to rigorously study the behavior of topological defects in LCs during phase transitions [42, 31, 43, 44], paving the way for deeper insights into fundamental properties of materials.

4. Experimental Section

Substrate preparation

ITO-coated glass substrates (SPI Supplies) are used to achieve uniform spreading of photosensitive dye. The glass is cut and cleaned using an ultrasonic cleaner with Hellmanex cleaning solution (Fisherbrand), followed by sequential rinsing with acetone, ethanol, and isopropyl alcohol. After rinsing, substrates are dried with N_2 gas. Photosensitive azo-dye Brilliant Yellow (BY, Sigma-Aldrich) was combined with n,n-dimethylformamide (DMF) to achieve a 1 wt.% solution. The BY-DMF solution is spin-coated onto the substrates at 3000 RPM for 45 seconds. After spin-coating, substrates are baked on a hot plate at 95°C for 15 minutes. All spin-coating and heating steps are performed in a humidity-controlled environment with relative humidity below 35% to optimize the BY thin film for photoalignment [45]. Substrates are subsequently fixed together using epoxy glue (Loctite) to create a liquid crystal cell. After the epoxy cures, we use spectroscopic reflectometry to measure the cells' thickness d, obtained from the absolute reflectance spectra (Oceanview) fit using custom Matlab code.

Photoalignment Instrumentation

The custom-built photo-patterning instrumentation consists of an LED source feeding into the side port of a bright-field inverted microscope body (TI Eclipse TE2000) as described previously in [31]. Projected images were designed in Keynote and generated using an LED-based projector (Sony MPL-C1A) connected to a peripheral optical path (*see Supplementary Information* Figure S2). The projector operates using three time-modulated laser diodes. We use the blue (λ = 445nm) diode to match the absorption band of the BY-DMF solution. Images generated by the projector first pass through two aspheric condenser lenses (Thorlabs, ACL50832U) with focal lengths f = 32 mm, separated by 64 mm. These lenses collimate the illumination. Two achromatic doublet lenses (f = 100 mm, Thorlabs, AC508-100-A-ML and f = 200 mm, Thorlabs, AC508-200-A-ML) bring the image into focus at the infinity-corrected plane near the microscope's side port. A removable linear polarizer is mounted directly before the side port. Once inside the microscope body, the image is reflected by a dichroic mirror, picked up by an infinity-corrected tube lens, and collected by a microscope objective (10x, Nikon E Plan, 0.25 NA) that focuses the light onto a BY-coated substrate.

Sample preparation and exposure process

To generate alignment boundary conditions, a large region of an azo-dye-coated substrate is exposed to linearly polarized blue light using the photoalignment ap-

paratus described above. When exposed to linearly polarized light, the photosensitive azo-dye molecules align orthogonal to the polarization plane, thereby determining the preferred azimuthal orientation of the nematic director, $\hat{n}$. To achieve spatial variation of the pretilt, we fill LC cells with 4-cyano-4'-pentylbiphenyl (5CB, Nematel GmbH). Once 5CB cools into the nematic phase, we re-expose the region to unpolarized light by eliminating the polarizer from the optical path. The pretilt is varied by varying the exposure duration across a region with unpolarized light. To fabricate lenses, spatially varying the exposure time is controlled by playing a movie in Keynote – crafted using custom Python code – to project an annular exposed region with a fixed outer radius and a time-varying inner radius as described above. After the photoalignment process is finished, LC cells are sealed on their ends using UV curable resin (Loon Outdoors UV Clear Fly Finish)

Polarized optical microscopy

We use a Nikon LV 100N Pol upright microscope to image photo-patterned regions. The microscope is equipped with a rotating stage and a 20x Nikon Tu Plan ELWD objective. Samples are placed on a heating stage (Instec HCS302) set to 23.4°C. Köhler illumination is achieved with a Nikon LW 0.65 condenser. A 647 nm bandpass filter (Thorlabs, FBH647-10) is used to restrict the incident wavelength of light for all measurements. Optical microscopy images are captured using a Nikon DS-Ri2 camera, with the adjustable aperture diaphragm lever of the condenser lens set to ≈ 0.1 to minimize stray light.

Jones Matrix Calculations for POM Texture Reconstruction

We use Jones calculus to qualitatively compare experimentally obtained polarized optical microscopy textures (POM) of gradient index (GRIN) lenses to those expected from the procedure to determine the pretilt profile $\beta(r)$ described above. The numerically derived director field is discretized into volume elements (voxels) on a 3D grid. Each position in the $x-y$ plane, denoted by $\boldsymbol{\rho}$, contains N voxels of thickness Δ stacked along the $z-$direction ($N\Delta = d$). Given that the change in $\hat{n}$ between consecutive voxels is small, we can infer that $\lambda \ll 1/|\nabla \hat{n}|$, where λ is the light's wavelength.

Each voxel, represented by ν, behaves as a uniaxial birefringent optical element. This is characterized by a 2×2 Jones matrix, $\mathcal{M}^{\nu}$, which depends on the extraordinary n_{e} and ordinary n_{o} refractive indices of the LC. The light's propagation through a voxel is subject to an n_{eff} that depends on the polar angle θ_{ν} between $\hat{n}$ and the light's propagation direction, $\boldsymbol{k}_0$. With $\boldsymbol{k}_0 = \hat{z}$, the plane of polarization is defined in the $x-z$ plane. The corresponding Jones matrix is expressed as:

$$\mathcal{M}^{\nu}(\boldsymbol{\rho}) \equiv \begin{pmatrix} e^{i n^{\nu}_{\mathrm{eff}}(\theta_{\nu}) 2\pi \frac{\Delta}{\lambda}} & 0 \\ 0 & e^{i n^{\nu}_{\mathrm{o}} 2\pi \frac{\Delta}{\lambda}} \end{pmatrix}. \tag{6}$$

Utilizing the refractive indices of 5CB at the experimental temperature and wavelength λ, we compute $\mathcal{M}^{\nu}(\boldsymbol{\rho})$. This allows us to construct a single operator, γ, which integrates the effects of all voxels at a given $\boldsymbol{\rho}$

Following the methodologies in [46] and [47], we establish 2×2 Jones matrices for both the polarizer, $\mathcal{P}$, and the analyzer, $\mathcal{A}$. The propagation of plane waves, $\boldsymbol{E_0}$, through the sequence of $\mathcal{P}$, $\gamma(\boldsymbol{\rho})$, and $\mathcal{A}$ results in a resultant Jones vector, $\boldsymbol{E}_T(\boldsymbol{\rho})$. The reconstructed POM texture is derived from the light intensity transmitted through each voxel, represented as $I_T(\boldsymbol{\rho}) = |\boldsymbol{E}_T(\boldsymbol{\rho})|^2$.

Acknowledgements

We thank Bastián Pradenas, Christina Ambrosino, Rocío Gonzalez, and Hillel Aharoni for their insights, assistance, and helpful discussions. Funding was provided by the NSF (DMR-2104747) and US-Israeli Binational Science Foundation BSF grant n.2018380 awarded to FS.

Conflict of Interest

The authors declare no conflict of interest.

References

[1] Gennes PGd, Prost J. The physics of liquid crystals. 2. ed., repr ed. No. 83 in International series of mono-

graphs on physics, Oxford: Clarendon Press; 2013.

[2] Ishihara S, Mizusaki M. Alignment control technology of liquid crystal molecules. Journal of the Society for Information Display 2019 Jul;28(1):44–74. https://doi.org/10.1002/jsid.825.

[3] Geary JM, Goodby JW, Kmetz AR, Patel JS. The mechanism of polymer alignment of liquid-crystal materials. Journal of Applied Physics 1987 Nov;62(10):4100–4108. https://doi.org/10.1063/1.339124.

[4] Chigrinov VG, Kozenkov VM, Kwok HS. Photoalignment of liquid crystalline materials: physics and applications. Wiley SID series in display technology, Chichester, England ; Hoboken, NJ: Wiley; 2008. OCLC: ocn225429570.

[5] Guo Y, Jiang M, Afghah S, Peng C, Selinger RLB, Lavrentovich OD, et al. Photopatterned Designer Disclination Networks in Nematic Liquid Crystals (Advanced Optical Materials 16/2021). Advanced Optical Materials 2021 Aug;9(16):2170063. https://onlinelibrary.wiley.com/doi/10.1002/adom.202170063.

[6] Muždalo A, Saalfrank P, Vreede J, Santer M. Cis-to-Trans Isomerization of Azobenzene Derivatives Studied with Transition Path Sampling and Quantum Mechanical/Molecular Mechanical Molecular Dynamics. Journal of Chemical Theory and Computation 2018;14(4):2042–2051. https://doi.org/10.1021/acs.jctc.7b01120, pMID: 29466663.

[7] Aleotti F, Nenov A, Salvigni L, Bonfanti M, El-Tahawy MM, Giunchi A, et al. Spectral Tuning and Photoisomerization Efficiency in Push–Pull Azobenzenes: Designing Principles. The Journal of Physical Chemistry A 2020;124(46):9513–9523. https://doi.org/10.1021/acs.jpca.0c08672, pMID: 33170012.

[8] Chigrinov V, Pikin S, Verevochnikov A, Kozenkov V, Khazimullin M, Ho J, et al. Diffusion model of photoaligning in azo-dye layers. Physical Review E 2004 Jun;69(6):061713. https://link.aps.org/doi/10.1103/PhysRevE.69.061713.

[9] Yaroshchuk O, Reznikov Y. Photoalignment of liquid crystals: basics and current trends. J Mater Chem 2012;22(2):286–300. http://dx.doi.org/10.1039/C1JM13485J.

[10] Chigrinov V, Muravski A, Kwok HS, Takada H, Akiyama H, Takatsu H. Anchoring properties of photoaligned azo-dye materials. Phys Rev E 2003;68:061702. https://doi-org.proxy1-bib.sdu.dk/10.1103/PhysRevE.68.061702.

[11] Kim J, Li Y, Miskiewicz MN, Oh C, Kudenov MW, Escuti MJ. Fabrication of ideal geometric-phase holograms with arbitrary wavefronts. Optica 2015 Nov;2(11):958. https://doi.org/10.1364/optica.2.000958.

[12] Seki T, Nagano S, Hara M. Versatility of photoalignment techniques: From nematics to a wide range of functional materials. Polymer 2013;54(22):6053–6072. https://www.sciencedirect.com/science/article/pii/S0032386113008410.

[13] Guo Y, Jiang M, Peng C, Sun K, Yaroshchuk O, Lavrentovich O, et al. High-Resolution and High-Throughput Plasmonic Photopatterning of Complex Molecular Orientations in Liquid Crystals. Advanced Materials 2016 Jan;28(12):2353–2358. https://doi.org/10.1002/adma.201506002.

[14] Culbreath C, Glazar N, Yokoyama H. Note: Automated maskless micro-multidomain photoalignment. Review of Scientific Instruments 2011 Dec;82(12). https://doi.org/10.1063/1.3669528.

[15] Wu H, Hu W, chao Hu H, wen Lin X, Zhu G, Choi JW, et al. Arbitrary photo-patterning in liquid crystal alignments using DMD based lithography system. Optics Express 2012 Jul;20(15):16684. https://doi.org/10.1364/oe.20.016684.

[16] Meng C, Wu JS, Smalyukh II. Topological steering of light by nematic vortices and analogy to cosmic strings. Nature Materials 2023 Jan;22(1):64–72. https://www.nature.com/articles/s41563-022-01414-y.

[17] Jiang M, Guo Y, Yu H, Zhou Z, Turiv T, Lavrentovich OD, et al. Low f-Number Diffraction-Limited Pancharatnam–Berry Microlenses Enabled by Plasmonic Photopatterning of Liquid Crystal Polymers. Advanced Materials 2019 Mar;31(18):1808028. https://doi.org/10.1002/adma.201808028.

[18] Ware TH, McConney ME, Wie JJ, Tondiglia VP, White TJ. Voxelated liquid crystal elastomers. Science 2015 Feb;347(6225):982–984. https://www.sciencemag.org/lookup/doi/10.1126/science.1261019.

[19] Wani OM, Zeng H, Wasylczyk P, Priimagi A. Programming Photoresponse in Liquid Crystal Polymer Actuators with Laser Projector. Advanced Optical Materials 2018 Jan;6(1):1700949. http://doi.wiley.com/10.1002/adom.201700949.

[20] Chen M, Hou Y, An R, Qi HJ, Zhou K. 4d printing of Reprogrammable Liquid Crystal Elastomers with Synergistic Photochromism And Photo-Actuation. Advanced Materials 2023 Jul;https://doi.org/10.1002/adma.202303969.

[21] Tseng MC, Fan F, Lee CY, Murauski A, Chigrinov V, Kwok HS. Tunable lens by spatially varying liquid crystal pretilt angles. Journal of Applied Physics 2011 Apr;109(8). https://doi.org/10.1063/1.3567937.

[22] Fan F, Srivastava AK, Du T, Tseng MC, Chigrinov V, Kwok HS. Low voltage tunable liquid crystal lens. Optics Letters 2013 Oct;38(20):4116. https://doi.org/10.1364/ol.38.004116.

[23] Bezruchenko VS, Muravsky AA, Murauski AA, Stankevich AI, Mahilny UV. Tunable Liquid Crystal Lens Based on Pretilt Angle Gradient Alignment. Molecular Crystals and Liquid Crystals 2016 Feb;626(1):222–228. https://doi.org/10.1080/15421406.2015.1106890.

[24] Lee YJ, Kim YK, Jo SI, Gwag JS, Yu CJ, Kim JH. Surface-controlled patterned vertical alignment mode with reactive mesogen. Optics Express 2009 Jun;17(12):10298. https://doi.org/10.1364/oe.17.010298.

[25] Babakhanova G, Turiv T, Guo Y, Hendrikx M, Wei QH, Schenning APHJ, et al. Liquid crystal elastomer coatings with programmed response of surface profile. Nature Communications 2018 Jan;9(1). http://dx.doi.org/10.1038/s41467-018-02895-9.

[26] Jiang M, Yu H, Feng X, Guo Y, Chaganava I, Turiv T, et al. Liquid Crystal Pancharatnam–Berry Micro-Optical Elements for Laser Beam Shaping. Advanced Optical Materials 2018 Oct;6(23). http://dx.doi.org/10.1002/adom.201800961.

[27] Chen P, Wei B, Hu W, Lu Y. Liquid-Crystal-Mediated Geometric Phase: From Transmissive to Broadband Reflective Planar Optics. Advanced Materials 2019 Sep;32(27). http://dx.doi.org/10.1002/adma.201903665.

[28] McGinty CP, Salvato T, Salvato Z, Kolacz J, Gotjen HG, Spillmann CM. Large, Tunable Liquid Crystal Pretilt Achieved by Enhanced Out-of-Plane Reorientation of Azodye Thin Films. Langmuir 2020 Jul;36(29):8554–8559. http://dx.doi.org/10.1021/acs.langmuir.0c01371.

[29] McGinty CP, Kołacz J, Spillmann CM. Large rewritable liquid crystal pretilt angle by in situ photoalignment of brilliant yellow films. Applied Physics Letters 2021 Oct;119(14):141111. https://doi.org/10.1063/5.0068726.

[30] Akiyama H, Kawara T, Takada H, Takatsu H, Chigrinov V, Prudnikova E, et al. Synthesis and properties of azo dye aligning layers for liquid crystal cells. Liquid Crystals 2002 Oct;29(10):1321–1327. https://doi.org/10.1080/713935610.

[31] Modin A, Ash B, Ishimoto K, Leheny RL, Serra F, Aharoni H. Tunable three-dimensional architecture of nematic disclination lines. Proceedings of the National Academy of Sciences 2023;120(27):e2300833120. https://www.pnas.org/doi/abs/10.1073/pnas.2300833120.

[32] Li J, Wu ST. Extended Cauchy equations for the refractive indices of liquid crystals. Journal of Applied Physics 2004 Jan;95(3):896–901. https://doi.org/10.1063/1.1635971.

[33] Kraan TC, van Bommel T, Hikmet RAM. Modeling liquid-crystal gradient-index lenses. Journal of the Optical Society of America A 2007 Oct;24(11):3467. http://dx.doi.org/10.1364/JOSAA.24.003467.

[34] Serra F, Gharbi MA, Luo Y, Liu IB, Bade ND, Kamien RD, et al. Curvature-Driven, One-Step Assembly of Reconfigurable Smectic Liquid Crystal "Compound Eye" Lenses. Advanced Optical Materials 2015 May;3(9):1287–1292. https://doi.org/10.1002/adom.201500153.

[35] Wani OM, Wasylczyk P, Priimagi A. Programming Photoresponse in Liquid Crystal Polymer Actuators with Laser Projector. Adv Opt Mater 2017;6:1700949.

[36] Zheng Z, Hu H, Zhang Z, Liu B, Li M, Qu DH, et al. Digital photoprogramming of liquid-crystal superstructures featuring intrinsic chiral photoswitches. Nature Photonics 2022 Mar;16(3):226–234. https://doi.org/10.1038/s41566-022-00957-5.

[37] Li SQ, Xu X, Veetil RM, Valuckas V, Paniagua-Domínguez R, Kuznetsov AI. Phase-only transmissive spatial light modulator based on tunable dielectric metasurface. Science 2019 Jun;364(6445):1087–1090. https://doi.org/10.1126/science.aaw6747.

[38] Schenning APHJ, Crawford GP, Broer DJ, editors. Liquid Crystal Sensors. CRC Press; 2017. https://doi.org/10.1201/9781315120539.

[39] He C, Chang J, Hu Q, Wang J, Antonello J, He H, et al. Complex vectorial optics through gradient index lens cascades. Nature Communications 2019 Sep;10(1). https://doi.org/10.1038/s41467-019-12286-3.

[40] Bielykh SP, Lucchetti L, Reshetnyak VY. Photoaligned Tunable Liquid Crystal Lenses with Parabolic Phase Profile. Crystals 2023 Jul;13(7):1104. https://doi.org/10.3390/cryst13071104.

[41] Hsiang EL, Yang Z, Yang Q, Lai PC, Lin CL, Wu ST. AR/VR light engines: perspectives and challenges. Advances in Optics and Photonics 2022 Nov;14(4):783. https://doi.org/10.1364/aop.468066.

[42] Aharoni H, Machon T, Kamien RD. Composite Dislocations in Smectic Liquid Crystals. Physical Review Letters 2017;118(25).

[43] Wang M, Li Y, Yokoyama H. Artificial web of disclination lines in nematic liquid crystals. Nature Communications 2017 Aug;8(1):388. https://www.nature.com/articles/s41467-017-00548-x.

[44] Yoshida H, Asakura K, Fukuda J, Ozaki M. Three-dimensional positioning and control of colloidal objects utilizing engineered liquid crystalline defect networks. Nature Communications 2015 May;6(1):7180. https://www.nature.com/articles/ncomms8180.

[45] Wang J, McGinty C, West J, Bryant D, Finnemeyer V, Reich R, et al. Effects of humidity and surface on photoalignment of brilliant yellow. Liquid Crystals 2017;44(5):863–872. https://doi.org/10.1080/02678292.2016.1247479.

[46] Hecht E. Optics. 5 ed ed. Boston: Pearson Education, Inc; 2017.

[47] Ellis PW, Pairam E, Fernández-Nieves A. Simulating optical polarizing microscopy textures using Jones calculus: a review exemplified with nematic liquid crystal tori. Journal of Physics D: Applied Physics 2019 May;52(21):213001. https://iopscience.iop.org/article/10.1088/1361-6463/ab08a7.